RSC Advances

PAPER

View Article Online
View Journal | View Issue

Cite this: *RSC Adv.*, 2026, **16**, 23884

Integrated triplex LFIA platform for decentralized molecular subtyping of breast cancer

Wenting Gao,[a] Iftak Hussain,[b] Theopisti A. Nikolaou,[a] Samantha Symons,[a] Ganga Dripaul,[a] Monalisa Almeida,[a] Yunting Guo,[b] Sally Adebamowo,[c] Clement Adebamowo *[c] and David Erickson *[bd]

Breast cancer is the most frequently diagnosed malignancy among women worldwide, with over 2.3 million new cases annually. Effective treatment relies on precise molecular subtyping, which stratifies tumors into categories such as Luminal A, Luminal B, HER2-enriched, and triple-negative breast cancer based on progesterone receptor (PR), estrogen receptor (ER), and human epidermal growth factor receptor 2 (HER2) expression. Despite its critical importance, subtyping remains largely inaccessible in low- and middle-income countries (LMICs) due to resource limitations, including the high cost and complexity of conventional diagnostic methods. Here, we present a rapid, portable, and cost-effective diagnostic platform that simultaneously quantifies PR, ER, and HER2 with high sensitivity and specificity. The system integrates a modular multiplex LFIA architecture, an incubation-enhanced reaction zone, and europium-based fluorescence detection with an automated, field-deployable imaging reader. These combined engineering features enable clinically relevant detection limits of 32 pM for PR, 76 pM for ER, and 25 pM for HER2, with cross-reactivity below 5%. Validation against enzyme-linked immunosorbent assay (ELISA) revealed strong correlation (R^2 > 0.95) across subtype-representative biomarker mixtures. Together, this integrated approach has the potential to enhance breast cancer diagnosis and management by addressing critical barriers to timely and accurate subtyping, providing a practical tool to support earlier intervention, expand access to personalized treatment, and improve patient outcomes in resource-limited settings.

Received 12th March 2026
Accepted 13th April 2026

DOI: 10.1039/d6ra02096h

rsc.li/rsc-advances

Introduction

Breast cancer remains the most prevalent cancer and a leading cause of cancer-related mortality among women worldwide. According to the latest 2025 World Health Organization (WHO) report, approximately 2.3 million new cases were diagnosed globally in 2022, with an estimated 670 000 deaths. Projections indicate that if current trends persist, annual cases will rise to 3.2 million by 2050, with mortality reaching 1.1 million.[1] Low- and middle-income countries (LMICs) will bear the brunt of this surge, where limited healthcare infrastructure and late-stage diagnoses contribute to disproportionately high mortality rates.[2] Alarmingly, in Africa, nearly 47% of breast cancer cases occur in individuals younger than 50 years, compared to significantly lower percentages in high-income regions such as North America (18%) and Europe (19%).[1] These disparities underscore the urgent need for accessible, affordable, and reliable diagnostic tools to facilitate early detection and timely intervention.

The molecular heterogeneity of breast cancer necessitates precise subtyping for effective therapeutic decisions and improved clinical outcomes.[3] Protein biomarkers such as estrogen receptor (ER), progesterone receptor (PR), and human epidermal growth factor receptor 2 (HER2) are essential for breast cancer classification into subtypes, including Luminal A, Luminal B, HER2-enriched, and triple-negative breast cancer (TNBC).[4,5] Accurate subtyping ensures selection of tailored treatment such as endocrine therapy for hormone receptor-positive (HR+) tumors and HER2-targeted therapies for HER2-positive cancers.[6,7] However, in LMICs, the high cost and limited availability of diagnostic infrastructure often result in delayed or absent molecular subtyping for breast cancer patients. This lack of timely and accurate subtyping restricts access to personalized treatment options and hinders effective prognostication, ultimately contributing to persistent global disparities in breast cancer care and patient outcomes.[8,9]

Conventional methods for biomarker detection, such as immunohistochemistry (IHC) and fluorescence *in situ* hybridization (FISH), remain the clinical gold standards for breast

[a]*Meinig School of Biomedical Engineering, Cornell University, Ithaca, NY, USA*
[b]*Sibley School of Mechanical and Aerospace Engineering, Cornell University, Ithaca, NY, USA. E-mail: de54@cornell.edu*
[c]*Greenebaum Comprehensive Cancer Center, Department of Epidemiology & Public Health, University of Maryland School of Medicine, Baltimore, MD, USA. E-mail: cadebamowo@som.umaryland.edu*
[d]*Division of Nutritional Sciences, Cornell University, Ithaca, NY, USA*

cancer subtyping.[5,6] These techniques, while widely used, are qualitative or semi-quantitative and rely on subjective interpretation of staining intensities, leading to significant inter-laboratory variability.[10,11] Moreover, IHC and FISH require substantial laboratory infrastructure and highly trained personnel, rendering them unavailable in many LMICs.[9,12,13] This limitation is particularly critical given that breast cancer in LMICs is often diagnosed at advanced stages, with survival outcomes significantly worse compared to high-income countries.[14,15]

Advances in quantitative protein detection technologies, such as enzyme-linked immunosorbent assays (ELISA) and mass spectrometry (MS), have enabled precise biomarker quantification in absolute picomolar (pM) ranges.[16–19] These technologies offer critical improvements over conventional IHC and FISH methods, providing objective and reproducible measurements of biomarker levels.[10,20,21] Quantitative thresholds derived from clinical and pathological studies have been established to distinguish breast cancer subtypes. Luminal A tumors, for instance, are characterized by high PR (>100 pM) and ER (>100 pM) expression, with low HER2 levels (<15–20 pM).[4,6,22] Luminal B tumors exhibit moderate PR (50–150 pM) and ER (50–200 pM) levels, with HER2 overexpression observed in HER2-positive cases (20–60 pM).[6,23,24] HER2-enriched cancers demonstrate high HER2 expression (>60 pM) and minimal PR/ER expression (<10 pM),[7,18,19,25] while TNBCs are characterized by the absence of all three biomarkers (<10 pM for PR, ER, and HER2).[20,24,26] These subtype-specific thresholds are directly tied to treatment strategies, such as endocrine therapy for HR+ tumors[6,22,27,28] or HER2-targeted therapies for HER2-positive cases, including trastuzumab and pertuzumab.[15,25,29–31]

Despite their clinical utility, quantitative technologies like ELISA and MS remain inaccessible for widespread use, particularly in LMICs, due to their high cost, reliance on sophisticated laboratories, and the need for specialized expertise. To address these challenges, we developed a portable, rapid, image-based detection system (PROVIDS)-enabled triplex lateral flow immunoassay (LFIA) capable of simultaneously quantifying PR, ER, and HER2 levels in a single assay. The triplex LFIA incorporates advanced features, including a pre-reaction zone for improved antigen–antibody interactions, europium-based fluorescence for strengthened sensitivity and specificity, and spatially separated test lines to eliminate cross-talk. The assay was engineered to span a clinically relevant dynamic range of 0–1000 pM, covering biomarker levels across all subtypes.[5,6] This range includes low biomarker concentrations required for TNBC detection (<10 pM)[20,24,26] and the higher levels characteristic of HR+ or HER2-enriched tumors, such as PR/ER > 100 pM or HER2 >60 pM.[5–7,32–34] In addition to these assay-level enhancements, the platform integrates directly with PROVIDS, a dedicated optical and computational reader that standardizes excitation, automates segmentation, and enables quantitative interpretation essential for subtype-relevant thresholding. This system-level integration transforms the assay from a qualitative strip into a clinically actionable, quantitative diagnostic capable of decentralized use. Taken together, this unified architecture represents, to our knowledge, the first decentralized triplex LFIA platform capable of clinically relevant breast cancer subtyping, providing a scalable and cost-effective solution that bridges critical diagnostic gaps in LMICs.

Results

Europium–streptavidin conjugates improve sensitivity and minimize background noise in LFIA

To enhance the sensitivity and performance of our LFIA system for detecting low-abundance biomarkers such as PR, ER, and HER2, europium–streptavidin (Eu–SA) conjugates were chosen over traditional gold nanoparticles-based (AuNP) systems due to their superior optical properties.[35–37] Unlike AuNPs, which rely on colorimetric detection and often suffer from low signal-to-background ratios, Eu–SA conjugates emit strong fluorescence when excited with UV light at 365 nm, with an emission peak at 610 nm.[37–40] This large stokes shift significantly reduces background noise, making Eu–SA conjugates ideal for highly sensitive immunoassays.[41,42]

To determine the optimal concentration of Eu–SA conjugates, we designed LFIA strips with biotinylated BSA immobilized at the capture site,[43] enabling quantification of fluorescence intensities under various Eu–SA concentrations (ranging from 0.001% to 1% solids, Fig. 1a). Increasing the Eu–SA concentration led to improved fluorescence intensity, indicating stronger signal amplification. However, background fluorescence also escalated at concentration beyond 0.005% solids, diminishing the signal-to-noise ratio. Thus, 0.005% solids was determined to be the optimal concentration of Eu–SA conjugates, providing robust signal amplification while minimizing background noise.

Next, we optimized the concentration of biotinylated detection antibodies for each biomarker. Proper antibody concentration is critical for efficient binding at the test line and reducing non-specific interactions.[42,44] Using 0.005% solids of Eu–SA conjugates, we tested detection antibody concentrations ranging from 0.005 mg mL^{-1} to 0.05 mg mL^{-1}, where biotinylated BSA was deposited at the capture site. Fluorescence intensity increased proportionally with higher antibody concentrations, peaking at 0.01 mg mL^{-1} for HER2 and 0.024 mg mL^{-1} for PR and ER (Fig. 1b). Beyond these thresholds, the fluorescence signal plateaued and non-specific binding increased, as reflected in the rise of background noise. Therefore, these concentrations were selected as the optimal values for biotinylated detection antibodies of each biomarker, ensuring an optimal balance between signal strength and background interference.

Subsequently, we optimized the concentration of donkey anti-immunoglobulin G (IgG) antibodies on the control line to capture any excess Eu–SA conjugates. The control line serves exclusively as a procedural validation of conjugate migration and reagent integrity by capturing excess Eu–streptavidin–biotinylated detection antibodies *via* host-species recognition. This optimization was necessary to ensure proper assay functionality and to prevent the accumulation of unbound conjugates. We tested donkey IgG concentrations ranging from 0.01 mg mL^{-1} to 0.25 mg mL^{-1}, with a fixed Eu–SA conjugated detection antibody

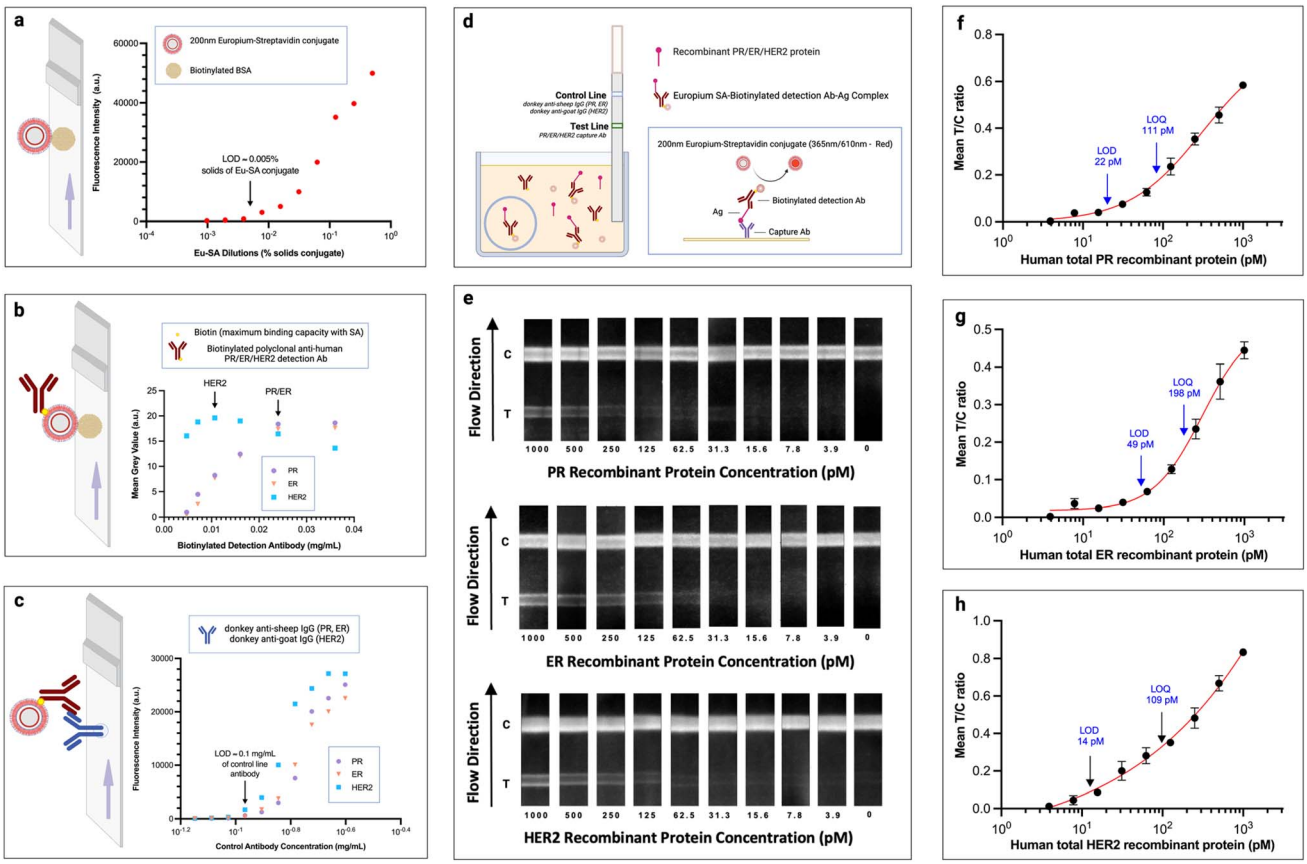

Fig. 1 Optimization and validation of Singleplex LFIA. (a) Fluorescence intensities obtained from nitrocellulose membranes, with biotinylated BSA as recognition elements at capture site, after exposure to various % solids of 200 nm europium–streptavidin conjugates. Inset: schematic illustration of streptavidin-conjugated europium (Eu–SA) nanoparticles. (b) Mean grey values obtained from nitrocellulose membrane, with biotinylated BSA as recognition elements at capture site, after exposure to the complex constitute of various concentration of biotinylated anti-human PR/ER/HER2 detection antibody with fixed % solids of Eu–SA conjugates. Inset: schematic illustration of [Eu–SA: biotinylated detection antibody] complex. (c) Fluorescence intensities obtained from nitrocellulose membranes, with various concentrations of polyclonal anti-human PR/ER/HER2 capture antibody as recognition element at capture site, after exposure to the same concentration of [Eu–SA: biotinylated detection antibody] complex as target analyte. Inset: schematic illustration of [Eu–SA: biotinylated detection antibody: capture antibody] complex. (d) Schematic illustration of individual LFIA strips compromising capture antibody test line and a donkey IgG control line. Inset: schematic illustration of the sandwich architecture of reagents at test line. (e) Fluorescence images of human total PR/ER/HER2 LFIAs. (f–h) Dose-dependent fluorescence intensities mean test-to-control (T/C) ratio curve of human total PR/ER/HER2 LFIAs. Lilac arrows indicate the direction of flow of the nanoconjugates. Data are mean ± s.d.; $n = 4$ repeated tests. Schematics were created with https://www.biorender.com/.

concentration for each biomarker. At 0.1 mg mL^{-1}, the control line efficiently captured unbound conjugates without affecting test line performance (Fig. 1c and e). Higher concentrations did not further improve the assay and contributed to increased background noise. Thus, 0.1 mg mL^{-1} was identified as the optimal concentration for the control line antibodies.

Finally, we fine-tuned the capture antibody concentrations for PR, ER, and HER2. Human total PR, ER, and HER2 capture antibodies, along with 0.1 mg mL^{-1} of donkey IgG antibodies, were immobilized on a nitrocellulose membrane to form test and control spots, respectively (Fig. 1d, SI Fig. S1a and b). For PR, we tested concentrations of 0.05 mg mL^{-1}, 0.1 mg mL^{-1}, and 0.5 mg mL^{-1} anti-human total PR capture antibodies. Offering a smooth sigmoidal curve without early saturation or fluctuating detection at lower concentrations (SI Fig. S1c). Similarly, for ER, concentrations of 0.18 mg mL^{-1}, 0.1 mg mL^{-1}, and 0.05 mg mL^{-1} anti-human total ER capture antibodies were evaluated, with 0.1 mg mL^{-1} showing optimal performance by avoiding the 0,0 early plateau observed at higher concentrations (SI Fig. S1d). For HER2, 0.36 mg mL^{-1} anti-human total HER2 capture antibodies proved ideal among the tested values of 0.1 mg mL^{-1}, 0.36 mg mL^{-1}, and 0.72 mg mL^{-1} tested concentrations, balancing strong signal amplification with minimal background noise (SI Fig. S1e). These optimizations ensure efficient antibody binding and minimize non-specific interactions across all biomarkers.

Bioanalytical parameters of singleplex LFIA dipsicks using Eu–SA conjugates

With the optimized concentrations of Eu–SA conjugates and antibodies, we evaluated the bioanalytical performance of singleplex LFIA by generating dose-response curves for PR, ER, and HER2. The key metrics assessed included the limit of detection

(LOD), limit of quantification (LOQ), and the assay's dynamic range, which are essential parameters for clinical utility. The clinically relevant range of 0–1000 pM was selected based on established levels of these biomarkers across various breast cancer subtypes, ensuring the assay's applicability in guiding treatment decisions. The LOD (mean + 3σ of the blank, where σ is the standard deviation) and LOQ (mean + 10σ of the blank) for each biomarker were calculated using a four-parameter logistic (4PL) model. Specifically, the LOD values for PR, ER, and HER2 were 22 pM, 49 pM, and 14 pM, respectively, indicating the assay's ability to detect even trace levels of these biomarkers. Meanwhile, LOQ values of 111 pM for PR, 198 pM for ER, and 109 pM for HER2 further validated the assay's precision for quantifying clinically relevant concentrations (Fig. 1f–h). The dose-response curves demonstrated high sensitivity of singleplex LFIA dipsticks across the full range of biomarker concentrations, spanning from low physiological levels to elevated disease-specific concentrations. Notably, greyscale values derived from 8-bit ImageJ-processed images of LFIA strips revealed that both dot- and line-based singleplex configurations exhibit similar LODs, suggesting no significant loss in assay specificity and sensitivity when transitioning to line-based dipstick format (SI Fig. 1c–e).

Effectiveness of the incubation pad in enhancing LFIA sensitivity

Conventional LFIA designs (SI Fig. S2a), which integrate conjugate and sample pads directly onto nitrocellulose membranes, often exhibit reduced sensitivity and reproducibility, particularly when detecting low-abundance analytes.[45,46] This limitation arises due to the rapid lateral flow mechanism, which shortens the antigen–antibody interaction time, preventing complete complex formation and reducing overall binding efficiency.[47,48] In our preliminary experiments, fluorescence signal intensities for PR, ER, and HER2 singleplex LFIA decreased by approximately 40% compared to the dipstick configuration (SI Fig. 2c–e). These findings underscore the critical need for design modifications to optimize interaction dynamics during assay operation.

To overcome these limitations, we introduced an incubation pad between the sample and conjugate pads (SI Fig. S2b).[49–51] This design creates a controlled pre-reaction zone, providing sufficient time for antigen–antibody binding before the sample entered the nitrocellulose membrane. By enabling near-equilibrium conditions, the incubation pad significantly enhances complex formation, restoring assay sensitivity to levels comparable to the dipstick configuration. Dose-response curves for PR, ER, and HER2 singleplex LFIA demonstrated smooth sigmoidal profiles, with LOD values of 24 pM, 62 pM, and 20 pM; and LOQ values of 133 pM, 213 pM, and 125 pM, respectively (Fig. 2b–d, singleplex; SI Table S1). These results align with the performance of the dipstick configuration, validating the effectiveness of the incubation pad. Additionally, fluorescence imaging of singleplex LFIA strips (SI Fig. S2f) confirmed the enhanced performance, with well-defined and consistent signals across test lines.

Dose-responsive behavior and sensitivity of triplex LFIA

Advancing upon the success of the singleplex LFIA, we extended the incubation pad design to create a triplex LFIA for simultaneous detection of PR, ER, and HER2 (Fig. 2a). While multiplexing enhances diagnostic efficiency, it introduces challenges such as competitive binding between analytes and variations in reaction kinetics, which can potentially compromise sensitivity and specificity.[52,53] The triplex architecture consists of three physically independent singleplex strips assembled in parallel with a 3 mm edge-to-edge spacing, each interfacing with a shared 10 mm × 18 mm sample pad through standardized 2 mm overlaps to ensure capillary flow while preventing lateral fluid crossover between membranes (SI Fig. S7). To assess whether the triplex configuration maintained sensitivity comparable to singleplex assays, we generated dose-response curves for PR, ER, and HER2 using serial dilutions of recombinant proteins spanning clinically relevant concentrations. These curves were fitted to the 4PL regression model, enabling the extraction of key parameters such as EC_{50}, which represents the concentration required to achieve 50% of the maximum signal.

The dose-response curves in the triplex LFIA retained the sigmoidal shape observed in singleplex assays, demonstrating robust signal dynamics across all biomarkers. For PR, the EC_{50} values were 2.497 pM (95% CI: 2.362–2.760) in singleplex and 2.588 pM (95% CI: 2.257–2.819) in triplex, with no statistically significant difference ($p > 0.05$). Similarly, ER exhibited EC_{50} values of 2.482 pM (95% CI: 2.384–2.663) in singleplex and 2.353 pM (95% CI: 2.268–2.481) in triplex assays. HER2, however, showed a slight increase in EC_{50}, rising from 3.206 pM (95% CI: 3.035–3.377) in singleplex to 4.945 pM (95% CI: 4.760–5.130) in triplex (SI Table S1). While this shift may reflect competitive interactions in the multiplexed format, overlapping confidence intervals confirm that sensitivity was not significantly compromised for any biomarker. Fluorescence imaging of the triplex LFIA (Fig. 2e) visually confirmed these findings, showing robust, well-defined test lines for PR, ER, and HER2. The distinct and uniform signal profiles across the dose range further validated the assay's capacity to maintain sensitivity under multiplexed conditions.

In addition to comparable EC_{50} values, the triplex LFIA exhibited consistent detection limits across biomarkers. The LOD were calculated as 32 pM for PR, 76 pM for ER, and 25 pM for HER2, while the LOQ were 154 pM, 250 pM, and 136 pM, respectively (Fig. 2b–d, triplex; SI Table S1). These values were consistent with singleplex assays, confirming the assay's capability to reliably detect and quantify biomarkers within clinically relevant ranges. Together, these results establish the triplex LFIA as a reliable platform for simultaneous detection without compromising individual biomarker sensitivity or quantification precision.

Cross-reactivity and specificity of triplex LFIA

Ensuring specificity in multiplexed assays requires rigorous evaluation of cross-reactivity, which occurs when nonspecific binding produces false-positive signals at unintended test

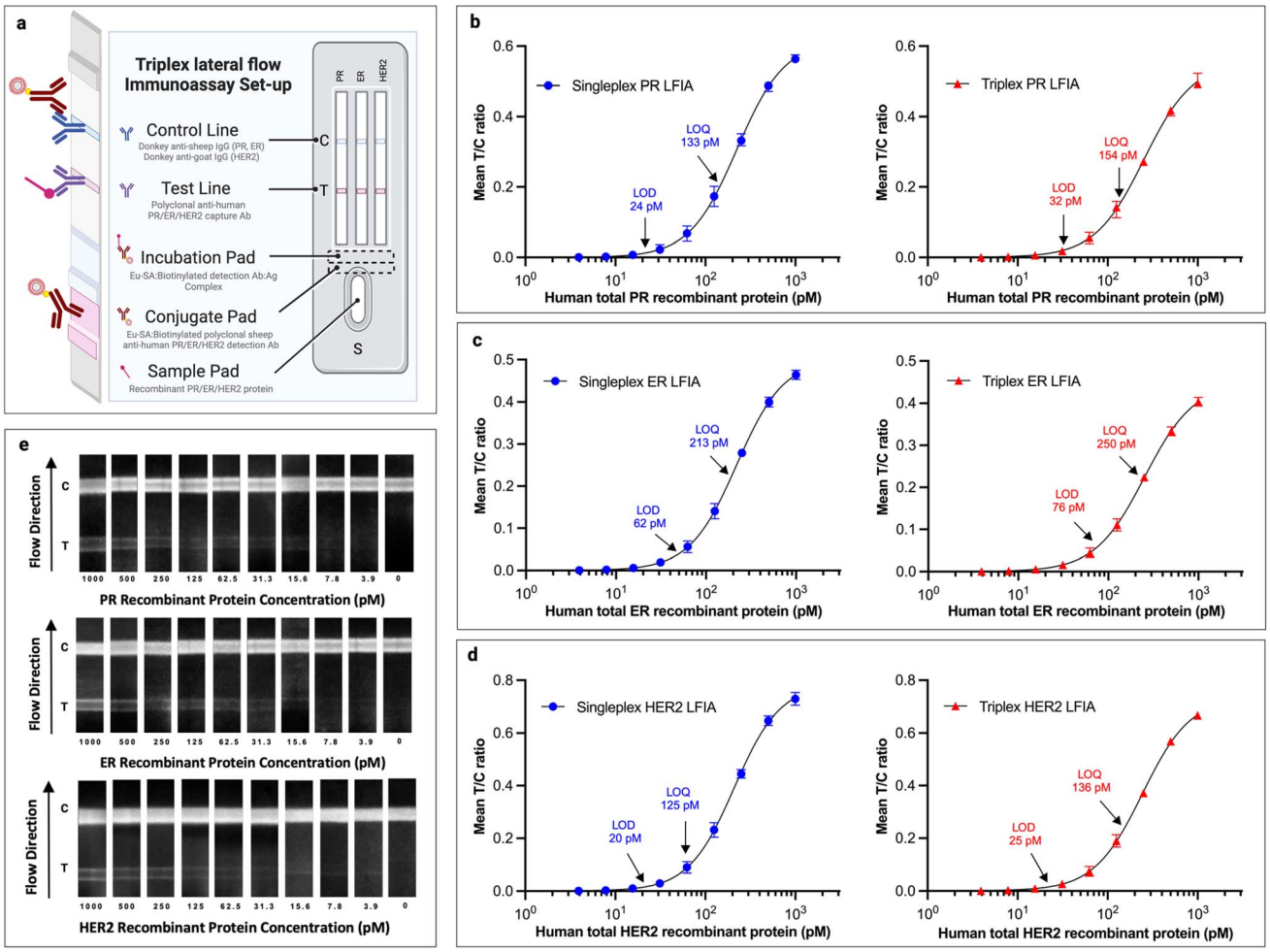

Fig. 2 Quantitative triplex LFIA of human PR/ER/HER2 proteins. (a) Schematic illustration of an optimized triplexplex sandwich LFIA compromising an absorption pad, a human total PR/ER/HER2 capture antibody test line, and a donkey IgG control line, assembled using three independent singleplex strips arranged with 3 mm strip-to-strip spacing to prevent lateral sample crossover, an [Eu–SA: biotinylated detection antibody] complex overspread conjugation pad, an incubation pad for enhanced assay reaction, and a sample pad for analyte and buffer addition. Inset: schematic illustration of the triplex LFIA incorporated with PR, ER, and HER2 LFIA. (b) Dose-dependent fluorescence intensities mean T/C ratio curve of singleplex and triplex human total PR LFIA. (c) Dose-dependent fluorescence intensities mean T/C ratio curve of singleplex and triplex human total ER LFIA. (d) Dose-dependent fluorescence intensities mean T/C ratio curve of singleplex and triplex human total HER2 LFIA. (e) Fluorescence images of human total PR/ER/HER2 triplex LFIAs (values for parameters can be found in Table S1). Data are mean ± s.d.; $n = 5$ repeated tests. Schematics were created with https://www.biorender.com/.

lines.[44,52] To comprehensively assess the specificity of the triplex LFIA, we tested edge-case conditions in which one biomarker was spiked at 1000 pM while the other two were absent. This design allowed us to evaluate the assay's ability to detect individual biomarkers accurately without interference from non-target analytes.

The triplex LFIA demonstrated high specificity, with cross-reactivity ratios consistently below 5% across all biomarkers and experimental conditions (SI Fig. S3; SI Table S2). When PR was spiked at 1000 pM, the PR test line exhibited a strong signal (35.98% ± 1.52%), while cross-reactivity at the ER and HER2 non-target test lines was minimal, at 3.41% (±0.81%) and 3.55% (±0.72%), respectively. Similarly, under ER spiking (1000 pM ER, 0 pM PR, 0 pM HER2), the ER test line displayed robust detection (31.14% ± 1.75%), with PR and HER2 test lines showing negligible cross-reactivity at 1.44% (±0.61%) and 3.31% (±0.61%), respectively. For HER2 spiking at 1000 pM, the HER2 test line showed the strongest response (50.96% ± 2.13%), while PR and ER test lines exhibited cross-reactivity ratios of only 1.21% (±0.54%) and 2.76% (±0.78%). These findings confirm that the triplex LFIA retains specificity comparable to singleplex assays ($p > 0.05$) and demonstrates reliable multiplexed detection with negligible nonspecific interactions.

The minimum asymptote (d) values derived from 4PL regression further validated these findings by quantifying baseline fluorescence in the absence of target analytes (SI Table S1). For PR, the d value in triplex was −0.01956 (95% CI: −0.1074 to 0.009142), aligning with the singleplex value of −0.001541 (95% CI: −0.02293 to 0.01436). Similarly, ER exhibited d values of

0.01717 (95% CI: 0.004127 to 0.02939) in triplex and 0.01390 (95% CI: −0.0004386 to 0.02618) in singleplex assays. HER2 showed consistent d values as well, with −0.06876 (95% CI: −0.1864 to 0.01635) in triplex and −0.07721 (95% CI: −0.3145 to 0.007079) in singleplex formats. The stability of d across all biomarkers reinforces the negligible nonspecific fluorescence observed in the triplex LFIA, underscoring its robust specificity. Together, these results confirm that both the physical strip spacing and the membrane-to-pad interface design effectively prevent lateral sample bleeding and maintain channel fidelity in the triplex format.

Multiplexed mixture validation and comparative benchmarking of triplex LFIA against ELISA

To translate the triplex LFIA system into a clinically actionable diagnostic tool, defining subtype-specific cutoffs for PR, HER2, and ER was essential. A comparative analysis was performed between the triplex LFIA and the laboratory-standard ELISA using recombinant biomarker mixtures. These mixtures were intentionally formulated to emulate subtype-representative concentration patterns, including both balanced and unbalanced combinations (*e.g.*, Luminal A: high PR/ER with low HER2; HER2-enriched: high HER2 with low PR/ER; and triple-negative conditions with all three markers low or absent), thereby assessing multiplex fidelity under mixed-analyte conditions rather than single-analyte spiking. Thirty recombinant protein samples per biomarker were prepared across physiologically relevant concentration ranges to mimic the molecular profiles of breast cancer subtypes. Each sample was tested with the triplex LFIA and parallel ELISA, generating paired datasets for statistical evaluation. Linear regression analysis demonstrated strong correlations between LFIA and ELISA results ($R^2 = 0.989$ for PR, $R^2 = 0.954$ for ER, and $R^2 = 0.995$ for HER2), underscoring the reliability of triplex LFIA measurements across a broad range of concentrations (Fig. 3a–c). Bland–Altman analysis quantified agreement between the methods, showing minimal biases (−0.21 pM for PR, −2.95 pM for ER, and +3.92 pM for HER2) and clinically acceptable 95% limits of agreement for all biomarkers (Fig. 3d–f). The precision of the triplex LFIA system was further characterized by root mean square error (RMSE) values of 14.9 pM for PR, 23.4 pM for ER, and 9.6 pM for HER2, highlighting its capability to quantify biomarker concentrations with minimal systematic error and acceptable variability. The agreement observed across these mixture conditions indicates that the analytical response of each channel scales with its cognate biomarker concentration even in the presence of co-analytes, supporting analytical independence of PR, ER, and HER2 in the multiplexed format.

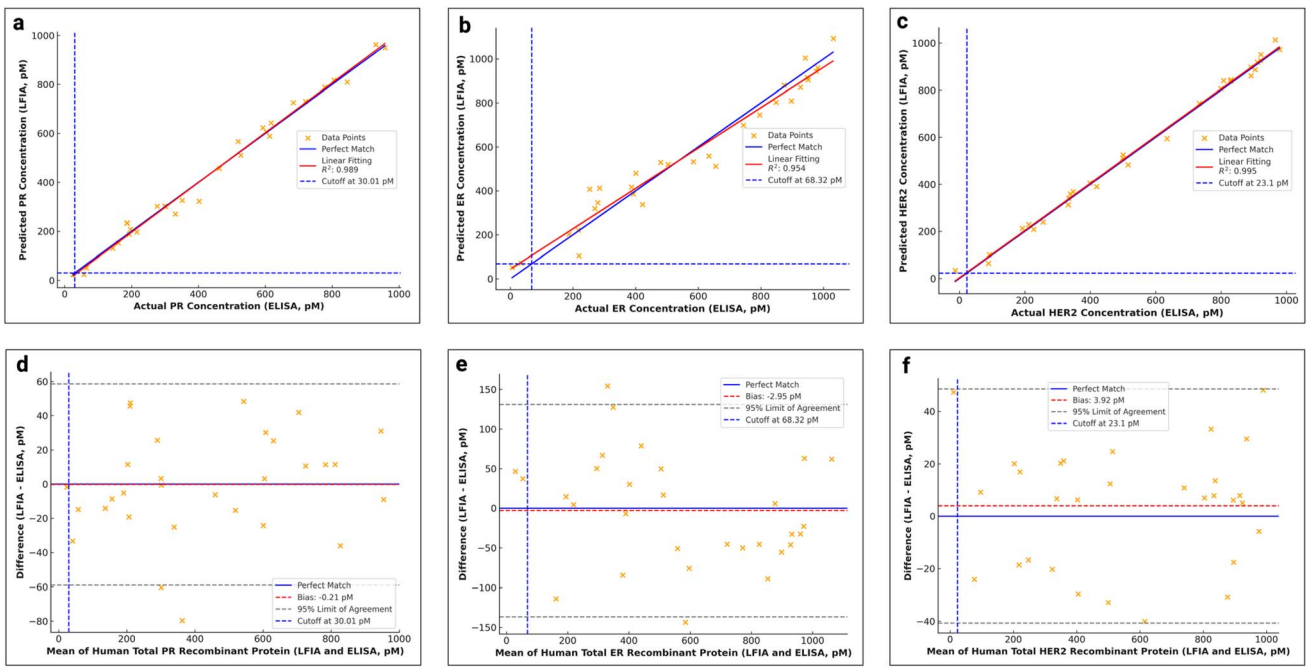

Fig. 3 Validation of PROVIDS-characterized concentrations of human breast cancer biomarkers. (a) Linear regression plot of human total PR concentrations acquired by triplex LFIAs from subtype-representative mixed biomarker samples and determined using PROVIDS built-in image processing code, and obtained by standard ELISA and determined by benchtop plate reader. Red line indicated RC = 1.017. Blue dashed line indicates cutoff at 30.01 pM. (b) Linear regression plot of human total ER concentrations acquired by triplex LFIAs and determined using PROVIDS built-in image processing code, and obtained by standard ELISA and determined by benchtop plate reader. Red line indicated RC = 0.958. Blue dashed line indicates cutoff at 68.32 pM. (c) Linear regression plot of human total HER2 concentrations acquired by triplex LFIAs and determined using PROVIDS built-in image processing code, and obtained by standard ELISA and determined by benchtop plate reader. Red line indicated RC = 1.038. Blue dashed line indicates cutoff at 23.1 pM. (d) Bland–Altman plot of human total PR test. The red dashed line indicates a bias at −0.21 pM. Blue dashed line indicates cutoff at 30.01 pM. (e) Bland–Altman plot of human total ER test. The red dashed line indicates a bias at −2.95 pM. Blue dashed line indicates cutoff at 68.32 pM. (f) Bland–Altman plot of human total HER2 test. The red dashed line indicates a bias at +3.92 pM. Blue dashed line indicates cutoff at 23.1 pM.

Subtype-specific cutoffs were then refined to reflect the detection capabilities of the triplex LFIA while aligning with clinical thresholds (SI Table S3). For PR, a lower detection limit of 30 pM was established, ensuring accurate classification of PR-positive subtypes (Luminal A: PR > 100 pM; Luminal B: PR 50–150 pM) and PR-negative subtypes (HER2-enriched, TNBC: PR < 30 pM). For ER, the lower limit of 68 pM was defined as the threshold for ER positivity, capturing Luminal A (ER > 100 pM) and Luminal B (ER 68–200 pM) while ensuring accurate classification of ER-negative subtypes (HER2-enriched, TNBC: ER < 68 pM). For HER2, a threshold of 23 pM distinguished HER2-negative subtypes (Luminal A, TNBC: HER2 < 23 pM) from HER2-positive subtypes (Luminal B: HER2 23–60 pM; HER2-enriched: HER2 > 60 pM). These refined cutoffs provide a statistically validated framework for future clinical studies and establish the triplex LFIA as a robust diagnostic platform.

Validation of triplex LFIA performance in human breast cancer lysates

To examine whether the expression patterns observed with recombinant standards translate to complex tissue-derived matrices, we evaluated two human breast cancer lysates with vendor-annotated molecular phenotypes (SI Table S5). Absolute PR, ER, and HER2 levels were quantified and positioned on the ELISA and triplex LFIA 4PL-derived calibration curves (SI Fig. S6a). In the ELISA panels, CP537436 (ER^+/PR^+) plotted at 140.8 pg mL^{-1} PR, 65.46 pg mL^{-1} ER, and 816.22 pg mL^{-1} HER2, consistent with its hormone-receptor-positive phenotype. In contrast, CP565605 ($HER2^+$) showed robust HER2 expression (2306.26 pg mL^{-1}) but PR and ER values below the ELISA LLOQ (reported as PR < 1.88 ng mL^{-1} and ER < 1.15 ng mL^{-1}), yielding no quantifiable PR/ER signal on the standard curves. Mapping the same lysates onto the triplex LFIA 4PL models produced recombinant-equivalent concentrations of 95.3, 45.8, and 29.4 pM for CP537436 and 41.3, 19.3, and 50.8 pM for CP565605 in the PR, ER, and HER2 channels, respectively. All PROVIDS-enabled triplex LFIA-derived values fell within the calibrated dynamic range and preserved the same inter-sample ordering observed by ELISA, providing a coherent analytical basis for the subsequent pattern-level and subtype-level comparisons.

To compare the two platforms on a unit-independent basis, PR/ER/HER2 expression values were normalized within each biomarker (SI Fig. S6b). This normalization yielded highly concordant expression hierarchies, whereby CP537436 consistently ranked as PR-high and ER-high (both normalizing to 1.00) with lower HER2 (0.38–0.58 across ELISA and triplex LFIA), and CP565605 presented the reciprocal HER2-dominant profile (HER2 normalizing to 1.00) with low-to-moderate PR and ER values (0.17–0.43 across ELISA and triplex LFIA). Notably, this directional agreement held even under conservative treatment of the CP565605 PR and ER values, which were normalized using their ELISA LLOQ upper bounds, reinforcing the robustness of the LFIA signal interpretation.

We next examined whether these patterns were sufficient to preserve subtype-level phenotypes (SI Fig. S6c). Both ELISA and triplex LFIA produced the same subtype signatures, with CP537436 exhibiting a PR-high/ER-high/HER2-low pattern and CP565605 showing the reciprocal PR-low/ER-low/HER2-high profile, demonstrating that the triplex format maintains biomarker hierarchy and subtype-defining structure in tissue lysates. Because subtype calls depend on the relative ordering rather than absolute units, the agreement between ELISA- and LFIA-derived signatures provides direct evidence that the quantitative behavior of the PROVIDS-enabled triplex LFIA extends beyond buffered standards to clinically relevant matrices.

Collectively, these findings show that triplex LFIA-derived concentrations fall within calibrated dynamic ranges, normalized expression profiles align tightly with ELISA across all biomarkers, and subtype-defining logic remains stable in tissue-derived samples. This establishes a strong foundation for the translational applicability of the PROVIDS-enabled triplex LFIA for subtype discrimination in real biological specimens.

Design and application of the PROVIDS reader for biomarker quantification

The Portable Rapid Onsite Versatile Image-based Detection System (PROVIDS) was developed to enable simultaneous quantification of PR, ER, and HER2 biomarkers (Fig. 4a). This system integrates a 3D-printed fluorescence imaging module to address the need for accessible, portable, and accurate diagnostic tools, especially in resource-limited settings. By combining high-performance optoelectronics, optimized hardware fabrication, and advanced image-processing algorithms, PROVIDS delivers reliable and precise biomarker quantification for clinical applications.

The PROVIDS system features a compact housing that integrates a high-resolution imaging module, a Raspberry Pi 4 board, and an LCD screen (Fig. 4b). The imaging module aligns precisely with the optical path of the LFIA test strips to ensure high image quality, with the Raspberry Pi serving as the computational core to control image acquisition and perform on-device analysis (Fig. 4c). The compact dimensions of 100 mm × 68 mm × 112 mm and a lightweight design (~290 grams) enhance portability. Powered by a 5000 mAh rechargeable battery, the system can operate continuously for over nine hours, supporting extended field use. The inclusion of a 32 GB microSD card enables efficient storage and retrieval of fluorescence image data, ensuring the system's utility in decentralized healthcare settings.

Key optoelectronic innovations in the PROVIDS system enhance its analytical performance. Six UV-LEDs with a peak emission wavelength of 365 nm provide the excitation light source, tailored to match the excitation wavelength of europium chelate microspheres used in the LFIA (Fig. 4d). A band-pass optical filter with a peak emission wavelength of 610 nm ensures the selective capture of fluorescence emission, effectively eliminating background noise. A Raspberry Pi high-quality camera (Sony IMX477 sensor, 4056 × 3040 pixels) records the fluorescence signals through an adjustable lens (Arducam LN038). The housing, fabricated using black

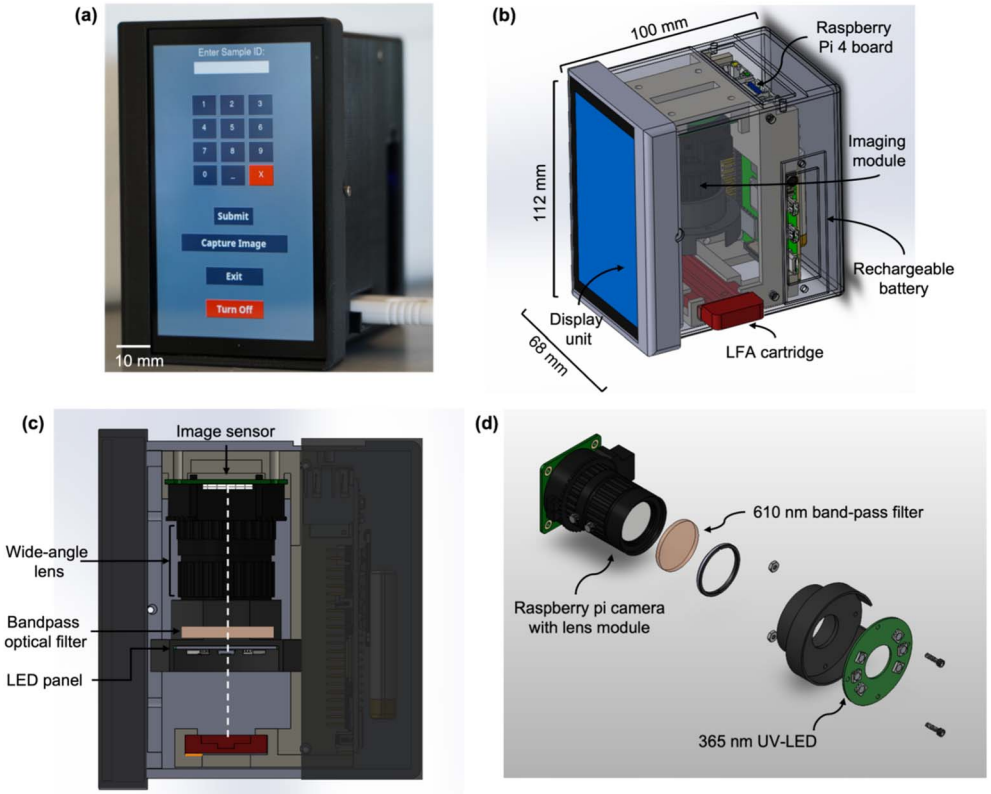

Fig. 4 PROVIDS hardware device for detection of fluorescent signals. (a) Photograph of the PROVIDS reader system with an LCD screen for sample ID entry, image capture, and system control. (b) 3D rendering of the PROVIDS system, showing its compact structure (100 mm × 68 mm × 112 mm) with key components including the Raspberry Pi 4 board, rechargeable battery, LFIA cartridge holder, and display unit. (c) Cross-sectional view of the optical assembly, highlighting the alignment of the lens, band-pass filter, and image sensor with the optical path of the LFIA cartridge for optimal fluorescence detection. (d) Schematic of the imaging module featuring a Raspberry Pi camera with an adjustable lens for high-resolution fluorescence imaging. The 610 nm band-pass filter isolates fluorescence emissions, and the 365 nm UV-LEDs provide excitation for europium chelate microspheres.

Polylactic Acid (PLA) filament, blocks external light interference, further enhancing signal precision and reproducibility.

The data acquisition and analysis pipeline for the PROVIDS system is automated by a Python-based application built in-house (SI Fig. S4). High-resolution images of LFIA test strips are captured under controlled lighting conditions, with the software isolating the region of interest (ROI) of each test strip for further processing. Horizontal intensity profiles extracted from the LFIA strips capture pixel intensity variations, which are smoothed using a Gaussian filter ($\sigma = 5$) to minimize outliers and reduce signal-to-noise ratio while preserving test and control line fluorescence profiles. Following this, test and control line peaks are automatically detected, background intensity is estimated as the mean pixel value between the two peaks. Background intensity is subtracted from the intensity profile to further reduce any remaining noise in the signal. Test (It) and control (Ic) line intensities are extracted from the background-subtracted profile, and their ratio correlates directly with biomarker concentration. A comprehensive end-to-end demonstration of the PROVIDS-enabled triplex LFIA workflow is provided in SI Materials and Methods and SI Video 1.

Subtype-specific cutoffs were defined to align the detection capabilities of the triplex LFIA with clinically validated thresholds for breast cancer subtyping (SI Table S3). These cutoffs enable the PROVIDS reader to quantitatively determine biomarker levels and classify samples into clinically relevant subtypes. When biomarker concentrations fall within the defined ranges, the PROVIDS reader provides both quantitative results and subtype classifications. If biomarker levels are below the lower detection limit, the system outputs the result as "< [cutoff concentration]," reflecting the absence or clinically negligible expression of the biomarker. The results, along with corresponding processed images and intensity profiles, are stored on the microSD card for retrieval. Details on the reporting format are provided in SI Fig. S5.

Discussion

The PROVIDS-enabled triplex LFIA platform offers a practical and scalable approach for improving access to breast cancer subtyping, particularly in LMICs where centralized testing capacity is limited. By integrating multiplexed detection into a portable and field-deployable format, the system addresses many of the logistical and infrastructural barriers that prevent timely determination of molecular subtype. The advancement presented here resides in the coordinated system-level

integration of assay architecture and quantitative analysis within a multiplex format. The platform's performance arises from the synergistic interaction of several engineered design features. The use of independently optimized PR, ER, and HER2 test strips housed within a unified triplex cassette helps avoid the steric interference and competitive binding that commonly reduce accuracy in co-printed multiplex layouts. An incubation-enhanced pre-reaction zone supports more complete antigen–antibody interactions prior to lateral flow, preserving the sensitivity typically achieved in singleplex assays. In addition, europium-based fluorescence combined with fixed spatial separation of test lines minimizes optical cross-talk and supports reliable signal differentiation across targets. Beyond these assay-level enhancements, the integration of PROVIDS transforms the device from a qualitative assay into a digitalized, quantitative diagnostic platform by enabling standardized excitation, automated image segmentation, and subtype-relevant interpretation suitable for decentralized use. Collectively, these elements establish a decoupled and quantitatively integrated multiplex architecture that preserves channel-level independence while enabling subtype-relevant threshold interpretation in a portable format.

Clinically, receptor determination for PR, ER, and HER2 under current ASCO/CAP clinical practice guidelines relies on tumor-derived tissue specimens obtained through core needle biopsy or surgical excision. Accordingly, the present platform is positioned not as a biopsy-free replacement modality, but as a decentralized quantitative alternative following standard tissue acquisition. This platform therefore has potential as a time-efficient and cost-effective tool for breast cancer subtyping in environments where diagnostic turnaround time and infrastructure constraints remain significant challenges. The modular tri-strip architecture further enhances manufacturing robustness by localizing variation to individual channels, enabling channel-specific quality control, requalification, or replacement without affecting the remaining components, a practical advantage over co-printed multiplex formats. Consolidating PR, ER, and HER2 assessment into one streamlined workflow reduces operational complexity and shortens the time to result, which may support more timely therapeutic decision-making. The assay's alignment with clinically relevant biomarker ranges enables identification of HER2-positive cases as well as hormone receptor-positive or triple-negative phenotypes, thereby complementing existing diagnostic pathways.

Importantly, the pilot evaluation using real patient-derived breast cancer tissue lysates provides direct evidence that the system's analytical logic holds in complex biological matrices. Across all six biomarkers, PROVIDS-enabled triplex LFIA-derived concentrations preserved the same inter-sample ordering observed by ELISA, and normalized expression profiles yielded nearly identical subtype-relevant hierarchies. Both lysates produced fully concordant subtype signatures, demonstrating preservation of clinically meaningful biomarker relationships rather than agreement at the level of recombinant-based units alone. These findings indicate that the platform maintains quantitative behavior and subtype-decision logic when evaluated using real tissue-derived samples, underscoring its translational relevance. Broader validation in real-world clinical settings will be important to assess robustness across diverse operational environments and patient populations.

Future work will focus on expanding the platform's capabilities, including the integration of additional biomarkers and on-strip tissue lysate purification, which may enable more comprehensive molecular phenotyping and simplify sample handling. Long-term field studies will also be essential for evaluating performance, usability, and clinical impact in decentralized healthcare environments. By combining analytical reliability with portability and scalability, the PROVIDS-enabled triplex LFIA platform represents a step toward more accessible diagnostic technologies and may help advance equitable breast cancer care in underserved regions.

Author contributions

C. A. and D. E. conceived and designed the study and secured funding for the project. W. G. and I. H. contributed equally as co-first authors, leading assay development, device integration, experimental design, data generation, quantitative analysis, and drafting of the manuscript. T. A. N. contributed to reader optimization, development of the digitalized image-processing workflow, and assisted with data collection and revision-stage analyses. S. S., G. D., M. A., Y. G., and S. A. assisted with data collection, experiment execution, and analysis. C. A. and D. E. also critically revised the manuscript and provided substantive feedback throughout the study. All authors reviewed, edited, and approved the final version of the manuscript.

Conflicts of interest

The authors declare that the study was conducted in the absence of any commercial or financial relationships that be construed as a potential conflict of interest.

Data availability

The datasets generated and/or analyzed during the current study are available in the Cornell eCommons repository under the title “Triplex Lateral Flow Immunoassay for Enhanced Molecular Subtyping of Breast Cancer”.

All custom image analysis code used in the PROVIDS system (LFIA Analyzer) for biomarker quantification is publicly available at https://github.com/d-ericksonlab/PROVIDS.

This study did not involve data collection from human subjects. All biomarker concentration data were generated using recombinant proteins and are fully shareable.

Supplementary information (SI): processed data for key figures—including calibration curves, cross-reactivity analyses, and sigmoidal curve fitting parameters for PR, ER, and HER2 quantification—are provided in the article's Supplementary Information (Fig. S1–S5; Tables S1–S3). See DOI: https://doi.org/10.1039/d6ra02096h.

Acknowledgements

This work was funded by NIH grants "Point of Care Diagnostic Test for Molecular Subtyping of Breast Cancer (PoCBreCa) Study" (Award Number: R21CA255835) and "Point of Care Technologies for Nutrition, Infection, and Cancer for Global Health (PORTENT)" (Award Number: U54EB034654). Additional support for C. A. and S. A. was provided by funds through the Maryland Department of Health's Cigarette Restitution Fund Program (CH-649-CRF) and the University of Maryland Greenebaum Cancer Center Support Grant (P30CA134274). The content is solely the responsibility of the authors and does not necessarily represent the official views of the National Institutes of Health or the Maryland Department of Health.

References

1 World Health Organization, *Global Breast Cancer Statistics 2025*, International Agency for Research on Cancer, Geneva, Switzerland, 2025, Available from: https://www.iarc.who.int/wp-content/uploads/2025/02/pr361_E.pdf. accessed [Mar 01, 2025].

2 J. Ferlay, M. Ervik, F. Lam, M. Laversanne, M. Colombet, L. Mery, M. Piñeros, A. Znaor, I. Soerjomataram and F. Bray *Global Cancer Observatory: Cancer Today (Version 1.1)*, International Agency for Research on Cancer, Lyon, France, 2024, Available from: https://gco.iarc.who.int/today, accessed [Feb 25, 2025].

3 F. Bray, *et al.*, Global cancer statistics 2022: GLOBOCAN estimates of incidence and mortality worldwide for 36 cancers in 185 countries, *Ca-Cancer J. Clin.*, 2024, **74**(3), 229–263.

4 T. Sørlie, *et al.*, Gene expression patterns of breast carcinomas distinguish tumor subclasses with clinical implications, *Proc. Natl. Acad. Sci. U. S. A.*, 2001, **98**(19), 10869–10874.

5 A. C. Wolff, *et al.*, Human Epidermal Growth Factor Receptor 2 Testing in Breast Cancer: American Society of Clinical Oncology/College of American Pathologists Clinical Practice Guideline Focused Update, *J. Clin. Oncol.*, 2018, **36**(20), 2105–2122.

6 K. H. Allison, *et al.*, Estrogen and Progesterone Receptor Testing in Breast Cancer: ASCO/CAP Guideline Update, *J. Clin. Oncol.*, 2020, **38**(12), 1346–1366.

7 S. Verma, *et al.*, Trastuzumab Emtansine for HER2-Positive Advanced Breast Cancer, *N. Engl. J. Med.*, 2012, **367**(19), 1783–1791.

8 P. Farmer, J. Frenk, F. M. Knaul, L. N. Shulman, G. Alleyne, L. Armstrong, R. Atun, D. Blayney, L. Chen, R. Feachem, M. Gospodarowicz, J. Gralow, S. Gupta, A. Langer, J. Lob-Levyt, C. Neal, A. Mbewu, D. Mired, P. Piot, K. S. Reddy, J. D. Sachs, M. Sarhan and J. R. Seffrin, Expansion of cancer care and control in countries of low and middle income: a call to action, *Lancet*, 2010, **376**(9747), 1186–1193.

9 V. Vanderpuye, *et al.*, An update on the management of breast cancer in Africa, *Infect. Agents Cancer*, 2017, **12**(1), 13.

10 T. Thambamroong, The concordance between IHC and ISH for HER-2 testing in breast cancer in Nakhon Pathom Hospital, Thailand, based on the ASCO/CAP 2018 guidelines: a retrospective study, *ecancermedicalscience*, 2022, **16**, 1370.

11 Z. Varga, *et al.*, Assessment of HER2 status in breast cancer: overall positivity rate and accuracy by fluorescence in situ hybridization and immunohistochemistry in a single institution over 12 years: a quality control study, *BMC Cancer*, 2013, **13**(1), 615.

12 M. Aznab, B. Izadi, F. Amirian, S. Khazaei, S. H. Madani and M. Ramezani, Comparison of Immunohistochemical Methods (IHC) and Fluorescent in Situ Hybridization (FISH) in the Detection of HER 2/Neu Gene in Kurdish Patients with Breast Cancer in Western Iran, *Int. J. Hematol. Oncol. Stem Cell Res.*, 2022, **16**(4), 217–223.

13 A. O. Kingham TP, V. Vanderpuye, C. Casper, F. A. Abantanga, T. B. Kamara, O. I. Olopade, M. Habeebu, F. B. Abdulkareem and L. Denny, Treatment of cancer in sub-Saharan Africa, *Lancet Oncol.*, 2013, **14**(4), e158–e167.

14 U.-S. K, Challenges to the early diagnosis and treatment of breast cancer in developing countries, *World J. Clin. Oncol.*, 2014, **5**(3), 465–477.

15 H. Sung, *et al.*, Global Cancer Statistics 2020: GLOBOCAN Estimates of Incidence and Mortality Worldwide for 36 Cancers in 185 Countries, *Ca-Cancer J. Clin.*, 2021, **71**(3), 209–249.

16 M. J. Ellis, *et al.*, Whole-genome analysis informs breast cancer response to aromatase inhibition, *Nature*, 2012, **486**(7403), 353–360.

17 J. P. L. Gonçalves, *et al.*, Characterization of Hormone Receptor and HER2 Status in Breast Cancer Using Mass Spectrometry Imaging, *Int. J. Mol. Sci.*, 2023, **24**(3), 2860.

18 W. D. Neagu AN, E. Buonanno, A. Jenkins, T. Alexa-Stratulat, B. I. Tamba and C. C. Darie, Proteomics and its applications in breast cancer, *Am. J. Cancer Res.*, 2021, **11**(9), 4006–4049.

19 S.-S. Kim, *et al.*, Quantifiable peptide library bridges the gap for proteomics based biomarker discovery and validation on breast cancer, *Sci. Rep.*, 2023, **13**(1), 8991.

20 A. Prat, *et al.*, Clinical implications of the intrinsic molecular subtypes of breast cancer, *Breast*, 2015, **24**, S26–S35.

21 E. A. Rakha, *et al.*, Retrospective observational study of HER2 immunohistochemistry in borderline breast cancer patients undergoing neoadjuvant therapy, with an emphasis on Group 2 (HER2/CEP17 ratio ≥2.0, HER2 copy number <4.0 signals/cell) cases, *Br. J. Cancer*, 2021, **124**(11), 1836–1842.

22 C. M. Perou, *et al.*, Molecular portraits of human breast tumours, *Nature*, 2000, **406**(6797), 747–752.

23 M. Dowsett, *et al.*, Assessment of Ki67 in Breast Cancer: Recommendations from the International Ki67 in Breast Cancer Working Group, *JNCI, J. Natl. Cancer Inst.*, 2011, **103**(22), 1656–1664.

24 L. A. Carey, *et al.*, The Triple Negative Paradox: Primary Tumor Chemosensitivity of Breast Cancer Subtypes, *Clin. Cancer Res.*, 2007, **13**(8), 2329–2334.

25 J. Dennis, G. M. C. Slamon, S. G. Wong, W. J. Levin, A. Ullrich and L. William, McGuire Human Breast Cancer: Correlation of Relapse and Survival with Amplification of the HER-2/neu Oncogene, *Science*, 1987, **235**, 177–182.

26 D. Huo, F. Ikpatt, A. Khramtsov, J. M. Dangou, R. Nanda, J. Dignam, B. Zhang, T. Grushko, C. Zhang, O. Oluwasola, D. Malaka, S. Malami, A. Odetunde, A. O. Adeoye, F. Iyare, A. Falusi, C. M. Perou and O. I. Olopade, Population differences in breast cancer: survey in indigenous African women reveals over-representation of triple-negative breast, *J. Clin. Oncol.*, 2009, **27**(27), 4515–4521.

27 Early Breast Cancer Trialists' Collaborative, G, Relevance of breast cancer hormone receptors and other factors to the efficacy of adjuvant tamoxifen: patient-level meta-analysis of randomised trials, *Lancet*, 2011, **378**(9793), 771–784.

28 Early Breast Cancer Trialists' Collaborative, G., Comparisons between different polychemotherapy regimens for early breast cancer: meta-analyses of long-term outcome among 100 000 women in 123 randomised trials, *Lancet*, 2012, **379**(9814), 432–444.

29 S. M. Swain, M. Shastry and E. Hamilton, Targeting HER2-positive breast cancer: advances and future directions, *Nat. Rev. Drug Discovery*, 2023, **22**(2), 101–126.

30 A. Prat, *et al.*, Molecular Features and Survival Outcomes of the Intrinsic Subtypes Within HER2-Positive Breast Cancer, *JNCI, J. Natl. Cancer Inst.*, 2014, **106**(8), dju152.

31 D.-Y. Oh and Y.-J. Bang, HER2-targeted therapies — a role beyond breast cancer, *Nat. Rev. Clin. Oncol.*, 2020, **17**(1), 33–48.

32 J. Baselga, *et al.*, Lapatinib with trastuzumab for HER2-positive early breast cancer (NeoALTTO): a randomised, open-label, multicentre, phase 3 trial, *Lancet*, 2012, **379**(9816), 633–640.

33 L. Gianni, *et al.*, Efficacy and safety of neoadjuvant pertuzumab and trastuzumab in women with locally advanced, inflammatory, or early HER2-positive breast cancer (NeoSphere): a randomised multicentre, open-label, phase 2 trial, *Lancet Oncol.*, 2012, **13**(1), 25–32.

34 N. M. Iyengar, *et al.*, Efficacy and Safety of Gemcitabine With Trastuzumab and Pertuzumab After Prior Pertuzumab-Based Therapy Among Patients With Human Epidermal Growth Factor Receptor 2–Positive Metastatic Breast Cancer, *JAMA Netw. Open*, 2019, **2**(11), e1916211.

35 I. Hemmilä and V. Laitala, Progress in Lanthanides as Luminescent Probes, *J. Fluoresc.*, 2005, **15**(4), 529–542.

36 X. Xia, *et al.*, Lateral Flow Immunoassay Using Europium Chelate-Loaded Silica Nanoparticles as Labels, *Clin. Chem.*, 2009, **55**(1), 179–182.

37 E. Juntunen, *et al.*, Performance of fluorescent europium(III) nanoparticles and colloidal gold reporters in lateral flow bioaffinity assay, *Anal. Biochem.*, 2012, **428**(1), 31–38.

38 K. Chen, *et al.*, A Rapid and Sensitive Europium Nanoparticle-Based Lateral Flow Immunoassay Combined with Recombinase Polymerase Amplification for Simultaneous Detection of Three Food-Borne Pathogens, *Int. J. Environ. Res. Publ. Health*, 2021, **18**(9), 4574.

39 F. Xia, *et al.*, Colorimetric detection of DNA, small molecules, proteins, and ions using unmodified gold nanoparticles and conjugated polyelectrolytes, *Proc. Natl. Acad. Sci. U. S. A.*, 2010, **107**(24), 10837–10841.

40 G. L. Mosley, *et al.*, Development of quantitative radioactive methodologies on paper to determine important lateral-flow immunoassay parameters, *Lab Chip*, 2016, **16**(15), 2871–2881.

41 L. Zhan, *et al.*, The Role of Nanoparticle Design in Determining Analytical Performance of Lateral Flow Immunoassays, *Nano Lett.*, 2017, **17**(12), 7207–7212.

42 C. Parolo, *et al.*, Tutorial: design and fabrication of nanoparticle-based lateral-flow immunoassays, *Nat. Protoc.*, 2020, **15**(12), 3788–3816.

43 P. C. Weber, D. H. Ohlendorf, J. Wendoloski and F. Salemme, Structural origins of high-affinity biotin binding to streptavidin, *Science*, 1989, **243**, 85–88.

44 G. A. Posthuma-Trumpie, J. Korf and A. Van Amerongen, Lateral flow (immuno)assay: its strengths, weaknesses, opportunities and threats. A literature survey, *Anal. Bioanal. Chem.*, 2009, **393**(2), 569–582.

45 L. Anfossi, *et al.*, Multiplex Lateral Flow Immunoassay: An Overview of Strategies towards High-throughput Point-of-Need Testing, *Biosensors*, 2018, **9**(1), 2.

46 J. D. Bishop, *et al.*, Sensitivity enhancement in lateral flow assays: a systems perspective, *Lab Chip*, 2019, **19**(15), 2486–2499.

47 P. Shah, X. Zhu and C.-Z. Li, Development of paper-based analytical kit for point-of-care testing, *Expert Rev. Mol. Diagn.*, 2013, **13**(1), 83–91.

48 X. Li, *et al.*, Microfluidic Paper-Based Sample Concentration Using Ion Concentration Polarization with Smartphone Detection, *Micromachines*, 2016, **7**(11), 199.

49 Y. Zhang, *et al.*, Improvement in Detection Limit for Lateral Flow Assay of Biomacromolecules by Test-Zone Pre-enrichment, *Sci. Rep.*, 2020, **10**(1).

50 Y. Deng, *et al.*, Recent advances in sensitivity enhancement for lateral flow assay, *Microchim. Acta*, 2021, **188**(11).

51 Z. Lu, *et al.*, Rapid diagnostic testing platform for iron and vitamin A deficiency, *Proc. Natl. Acad. Sci. U. S. A.*, 2017, **114**(51), 13513–13518.

52 A. A. Ellington, I. J. Kullo, K. R. Bailey and G. G. Klee, Antibody-based protein multiplex platforms: technical and operational challenges, *Clin. Chem.*, 2010, **56**(2), 186–193.

53 S. F. Kingsmore, Multiplexed protein measurement: technologies and applications of protein and antibody arrays, *Nat. Rev. Drug Discovery*, 2006, **5**(4), 310–321.